ECCOMAS Congress 2016
VII European Congress on Computational Methods in Applied Sciences and Engineering
M. Papadrakakis, V. Papadopoulos, G. Stefanou, V. Plevris (eds.)
Crete Island, Greece, 5–10 June 2016

THREE-DIMENSIONAL CRACK PROPAGATION ANALYSIS USING MESHLESS POINT COLLOCATION METHOD

Eiji Tanaka[1]

[1]Institute of Technology, Shimizu Corporation
3-4-17 Etchujima, Koto-ku, Tokyo 135-8530 Japan
e-mail: tanaka_e@shimz.co.jp

Keywords: Point collocation method, Meshless methods, Constrained moving least squares approximation, crack propagation, cohesive crack

Abstract. *This paper presents a meshless point collocation method for three-dimensional crack propagation. The meshless point collocation method is based on direct discretization of strong-form governing equations to achieve a truly meshless scheme that does not require mesh structures or a numerical integration procedure. These characteristics of the point collocation method enable the direction of an arbitrary crack propagation to be defined purely according to the fracture criterion of the mechanical model because node-wise topology can be easily transformed by the simple addition of nodes and polygonal surfaces. The main advantages of the presented method are that there is no need to consider the consistency between the mesh connectivity and continuity of fracture zone locations and that the crack propagation procedure is relatively simplified with no additional implementation features from numerical integration used in weak formulations. The constrained moving least squares approximation (C-MLS) is employed for meshless interpolation so that essential boundary conditions can easily be applied. A cohesive crack model is directly introduced in combination with the crack growth procedure to express the fracture of quasi-brittle materials such as concrete. The accuracy and robustness of the presented method were demonstrated through its application to several numerical examples.*

1 INTRODUCTION

The meshless method is an attractive numerical technique that can solve various natural phenomena and engineering problems that conventional mesh methods are not applicable to. To date, a number of computational methods have appeared, such as smoothed particle hydrodynamics (SPH) [1, 2], the diffuse element method (DEM) [3], the element-free Galerkin method (EFGM) [4], the reproducing kernel particle method (RKPM) [5], and the partition of unity finite element method (PUFEM) [6]. Although these meshless methods have been applied to various engineering problems and become popular in computational mechanics, each still exhibits several disadvantages. Some are not completely meshless and use background meshes or other mesh structures over the problem domain because of the numerical integration in weak-form governing equations. Most also have difficulties with treating essential boundary conditions because of the lack of interpolation properties. For example, the moving least squares approximation (MLS) [7] lacks the Kronecker delta property. Further research is required on meshless methods to overcome these issues.

The point collocation approach—of which examples include the finite point method (FPM) [8], meshfree point collocation method (MPCM) [9], and particle difference method (PDM) [10]—is known to achieve a completely meshless method based on node-wise strong formulation. There are two characteristics to transforming the point collocation approach into a truly meshless method: using strong-form governing equations to avoid any complex implementation features caused by the numerical integration scheme of the weak formulation and using interpolation schemes that do not require meshes to construct shape functions, such as the reproducing kernel approximation and MLS approximation. Compared to other meshless methods, the point collocation approach is a relatively simple scheme because most meshless methods need some additional mesh structures or numerical integration procedure. Point collocation methods have been applied to fluid flow problems [8], elasticity of solid mechanics [11], solid elastoplasticity [12, 13], and crack growth problems [14] in two dimensions.

This paper presents a meshless point collocation method for the analysis of three-dimensional fracture. The constrained moving least squares (C-MLS) approximation, which is a meshless interpolation technique proposed by Noguchi et al. [15, 16], is introduced to easily treat essential boundary conditions. The topological change due to crack propagation is simply represented by the addition and subtraction of nodes and surfaces. A cohesive crack model is employed to deal with the fracture of quasi-brittle materials such as concrete. The cohesive crack model suggested by Barenblatt [17] is widely exploited to address the fracture of engineering materials to which classical linear fracture mechanics cannot be applied. The cohesive crack model assumes that a virtually narrow band called the cohesive zone exists ahead of a crack tip and represents the fracture process zone. The resistance to fracture is considered to be a gradual process in which separation between incipient crack surfaces is given by the cohesive traction of the cohesive zone following a cohesive constitutive law. The cohesive constitutive law represents the failure characteristics of the materials and is governed by cohesion at the atomistic scale, crack-bridging ligaments, interlocking of grains, and other factors. Crack growth occurs when the cohesive traction applied to the outer end of the cohesive zone disappears. Several numerical examples were considered, and the results were compared with those in the literature.

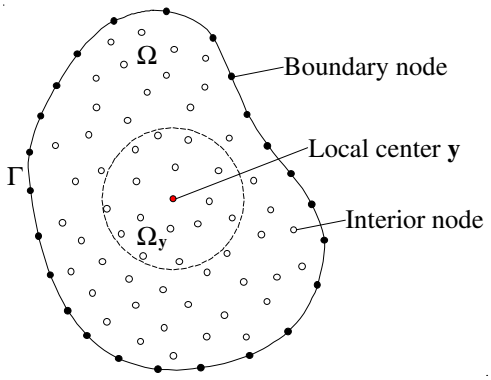

Figure 1: Support domain Ω_y for C-MLS approximation of the local center $\mathbf{y}$

2 ANALYSIS METHODS

2.1 Constrained moving least squares approximation

This section introduces the C-MLS approximation procedure with some extensions and modifications based on the original scheme [15, 16]. Consider a domain Ω surrounded by a boundary Γ in $\mathbb{R}^n$, as shown in Fig. 1. Suppose that a continuous function $u(\mathbf{x}) : \bar{\Omega} \to \mathbb{R}$ is to be approximated and that the nodal values u_I at $\mathbf{x}_I \in \bar{\Omega}$, $I = 1,2,...,N$ are given, where N is the number of nodes included in the support domain $\bar{\Omega}$. For the sake of convenience, multi-index notation has been adopted. Let $\mathbf{x} = (x_1,...,x_n)$ be an n-dimensional vector and $\boldsymbol{\alpha} = (\alpha_1,...,\alpha_n)$ be an n-tuple of non-negative integers. Then, the αth power of $\mathbf{x}$ is interpreted as $\mathbf{x}^{\boldsymbol{\alpha}} = x_1^{\alpha_1} x_2^{\alpha_2} \dots x_n^{\alpha_n}$ and $|\boldsymbol{\alpha}| = \sum_{i=1}^{n} \alpha_i$. In addition, $D_{\mathbf{x}}^{\boldsymbol{\alpha}} := \partial_{x_1}^{\alpha_1} \partial_{x_2}^{\alpha_2} \dots \partial_{x_n}^{\alpha_n}$ indicates the αth partial derivative operator with respect to $\mathbf{x}$. The αth derivative of the differentiable function $f(\mathbf{x})$ is given by

$$D_{\mathbf{x}}^{\boldsymbol{\alpha}} f(\mathbf{x}) = \frac{\partial^{|\boldsymbol{\alpha}|} f(\mathbf{x})}{\partial_{x_1}^{\alpha_1} \partial_{x_2}^{\alpha_2} \dots \partial_{x_n}^{\alpha_n}}. \tag{1}$$

The C-MLS approximation employs an approximate function based on a Taylor series instead of the normal polynomial approximation used in general MLS. The local approximation of $u(\mathbf{x})$ derived from the mth order Taylor polynomial is written as

$$u^h(\mathbf{x},\mathbf{y}) = u_{\mathbf{y}} + \mathbf{p}_m^T(\mathbf{x},\mathbf{y})\mathbf{a}(\mathbf{y}) \tag{2}$$

where $\mathbf{p}_m^T$ is constructed from all of the elements in the set $\mathscr{P}_m = \left\{ (\mathbf{x}-\mathbf{y})^{\boldsymbol{\alpha}}/\boldsymbol{\alpha}! \;\middle|\; \boldsymbol{\alpha} \in \mathscr{A}_m \right\}$, $\mathbf{a}(\mathbf{y})$ is the corresponding unknown coefficient vector made from the elements in the set $\mathscr{D}_m = \left\{ D_{\mathbf{x}}^{\boldsymbol{\alpha}} u(\mathbf{y}) \;\middle|\; \boldsymbol{\alpha} \in \mathscr{A}_m \right\}$, and $\mathscr{A}_m = \left\{ \boldsymbol{\alpha} \;\middle|\; 1 \le |\boldsymbol{\alpha}| \le m \right\}$. In addition, the number of all elements in the set $\mathscr{A}_m$ is $L = (n+m)!/(n!m!) - 1$. The above equation implies that a constraint condition is imposed on the approximate function used in MLS approximation, and all of the derivative approximations for $u(\mathbf{y})$ up to the mth order are obtained by $\mathbf{a}(\mathbf{y})$. In the sense of a discrete L_2 norm, the residual J is defined by

$$J = \sum_{I=1}^{N} w\left(\frac{\mathbf{x}_I - \mathbf{y}}{\rho_{\mathbf{y}}} \right) \left[\mathbf{p}_m^T(\mathbf{x}_I,\mathbf{y})\mathbf{a}(\mathbf{y}) + u_{\mathbf{y}} - u_I \right]^2 \tag{3}$$

where w is the support of the weight function and $\rho_{\mathbf{y}}$ (i.e., the dilation parameter) determines the size of the support domain $\bar{\Omega}$. The best local approximation is derived by minimizing the

functional $J(\mathbf{y})$ in Eq. (3) under the stationary condition. This yields the following normal equation:

$$\mathbf{a}(\mathbf{y}) = \mathbf{M}^{-1}(\mathbf{y})\mathbf{B}(\mathbf{y})\mathbf{u} \tag{4}$$

$$\mathbf{M}(\mathbf{y}) = \sum_{I=1}^{N} w\left(\frac{\mathbf{x}_I - \mathbf{y}}{\rho_{\mathbf{y}}}\right)\mathbf{p}_m(\mathbf{x}_I,\mathbf{y})\mathbf{p}_m^T(\mathbf{x}_I,\mathbf{y}) \tag{5}$$

$$\mathbf{B}(\mathbf{y}) = \left(w\left(\frac{\mathbf{x}_1 - \mathbf{y}}{\rho_{\mathbf{y}}}\right)\mathbf{p}_m(\mathbf{x}_1,\mathbf{y}),\ldots,w\left(\frac{\mathbf{x}_N - \mathbf{y}}{\rho_{\mathbf{y}}}\right)\mathbf{p}_m(\mathbf{x}_N,\mathbf{y})\right) \tag{6}$$

where $\mathbf{u} = (u_1 - u_{\mathbf{y}}, u_2 - u_{\mathbf{y}}, \ldots, u_N - u_{\mathbf{y}})^T$. The local approximation of $u(\mathbf{x})$ is interpreted as

$$u^h(\mathbf{x},\mathbf{y}) = u_{\mathbf{y}} + \mathbf{p}_m^T(\mathbf{x},\mathbf{y})\mathbf{M}^{-1}(\mathbf{y})\mathbf{B}(\mathbf{y})\mathbf{u}. \tag{7}$$

Thus, the C-MLS approximation clearly satisfies $u^h(\mathbf{y},\mathbf{y}) = u_{\mathbf{y}}$ because a constraint condition is imposed, which means that no special implementation is required to treat the essential boundary conditions. These are the distinctive characteristics of C-MLS compared to MLS [7] and other approximation schemes.

Consider the derivative approximation of $u(\mathbf{x})$ at the local center $\mathbf{y}$. Then, the derivative coefficients of the Taylor polynomial can be related to differentiation with respect to $\mathbf{x}$ by substituting $\mathbf{x} = \mathbf{y}$ as $D_{\mathbf{x}}^{\boldsymbol{\alpha}} u^h(\mathbf{x},\mathbf{y})\big|_{\mathbf{x}=\mathbf{y}} \approx D_{\mathbf{x}}^{\boldsymbol{\alpha}} u(\mathbf{y}) = D_{\mathbf{x}}^{\boldsymbol{\alpha}} u(\mathbf{x})$. Equation (4) is transformed as shown below:

$$\begin{pmatrix} D_{\mathbf{x}}^{\boldsymbol{\alpha}_1} u(\mathbf{x}) \\ \vdots \\ D_{\mathbf{x}}^{\boldsymbol{\alpha}_L} u(\mathbf{x}) \end{pmatrix} = \begin{pmatrix} \Phi_1^{[\boldsymbol{\alpha}_1]}(\mathbf{x}) & \ldots & \Phi_N^{[\boldsymbol{\alpha}_1]}(\mathbf{x}) \\ \vdots & \ddots & \vdots \\ \Phi_1^{[\boldsymbol{\alpha}_L]}(\mathbf{x}) & \ldots & \Phi_N^{[\boldsymbol{\alpha}_L]}(\mathbf{x}) \end{pmatrix} \begin{pmatrix} u_1 \\ \vdots \\ u_N \end{pmatrix} \tag{8}$$

where $\boldsymbol{\alpha}_1,\ldots,\boldsymbol{\alpha}_L$ are the elements in the set $\mathscr{A}_m$ sorted in a lexicographic order and $\Phi_I^{[\boldsymbol{\alpha}_K]}(\mathbf{x})$ denotes the $\boldsymbol{\alpha}_K$th derivative of the nodal shape function. If K is omitted, $\Phi_I^{[\boldsymbol{\alpha}_K]}(\mathbf{x})$ is expressed as

$$\Phi_I^{[\boldsymbol{\alpha}]}(\mathbf{x}) = \mathbf{e}_{\boldsymbol{\alpha}}^T \mathbf{M}^{-1}(\mathbf{x})\mathbf{c}_I(\mathbf{x}) \tag{9}$$

$$\mathbf{c}_I(\mathbf{x}) = \begin{cases} w\left(\dfrac{\mathbf{x}_I - \mathbf{x}}{\rho_{\mathbf{x}}}\right)\mathbf{p}_m(\mathbf{x}_I,\mathbf{x}) & \text{for } \mathbf{x}_I \neq \mathbf{x} \\ -\displaystyle\sum_{\mathbf{x}_I \neq \mathbf{x}} w\left(\dfrac{\mathbf{x}_I - \mathbf{x}}{\rho_{\mathbf{x}}}\right)\mathbf{p}_m(\mathbf{x}_I,\mathbf{x}) & \text{for } \mathbf{x}_I = \mathbf{x} \end{cases} \tag{10}$$

where $\mathbf{e}_{\boldsymbol{\alpha}}^T = (0,\ldots,1,\ldots,0)$ is a unit vector of the same order as the polynomial basis, whose non-zero component is related to the $\boldsymbol{\alpha}$th derivative. Then the derivative approximation $D_{\mathbf{x}}^{\boldsymbol{\alpha}} u(\mathbf{x})$ is given by

$$D_{\mathbf{x}}^{\boldsymbol{\alpha}} u(\mathbf{x}) = \sum_{I=1}^{N} \Phi_I^{[\boldsymbol{\alpha}]}(\mathbf{x}) u_I. \tag{11}$$

Therefore, C-MLS does not need direct differentiation of the shape function, which is a costly process in most meshless methods. This means that the computation speed for the derivatives can be considerably improved, especially when computing high-order derivative approximations.

The weight function used in all numerical calculations is non-smooth and is given as follows:

$$w(\mathbf{r}) = \begin{cases} \left(1 - \|\mathbf{r}\|^{\frac{1}{2}}\right)^2 & \text{for } \|\mathbf{r}\| \leq 1 \\ 0 & \text{for } \|\mathbf{r}\| > 1 \end{cases} \tag{12}$$

where $\mathbf{r} = (\mathbf{x}_I - \mathbf{x})/\rho_{\mathbf{x}}$. Although several numerical methods based on MLS approximation require a differentiable weight function to approximate the derivatives, C-MLS does not need the weight function to be differentiable because the derivative of the approximation includes no derivatives of the weight function. Yoon [10] stated that non-smooth functions are more suitable for strongly formulated meshless methods than smooth ones.

The dilation parameter $\rho_{\mathbf{x}}$ indicates the support radius of the weight function and how many nodes are included in the local approximation. Although some early meshless methods used a constant radius probe regardless of the node density [4, 5], several surveys [18] have noted that this may affect the approximation and suggested the variable dilation parameter to adjust the support range depending on the position of the local center and node density. In the present work, $\rho_{\mathbf{x}}$ was chosen to maximize the support radius under the condition $N \leq 7.89L$ where $m = n = 3$.

2.2 Point collocation scheme

Next, the framework of the point collocation method based on the strong formulation is explained. Let Ω be a bounded domain in $\mathbb{R}^n$ with the boundary Γ, as shown in Fig. 1. Then, the nonlinear problem is governed by the following set of partial differential equations:

$$\mathsf{A}_\Omega \mathbf{u} = \mathbf{f}_\Omega \quad \text{in } \Omega \tag{13}$$

$$\mathsf{A}_\Gamma \mathbf{u} = \mathbf{f}_\Gamma \quad \text{on } \Gamma \tag{14}$$

where A_Ω denotes the partial differential operator of the given problem and A_Γ denotes the boundary value operator for the boundary condition. The above equations can be interpreted as

$$\mathbf{r}_\Omega(\mathbf{u}) = \mathsf{A}_\Omega \mathbf{u} - \mathbf{f}_\Omega = \mathbf{0} \quad \text{in } \Omega \tag{15}$$

$$\mathbf{r}_\Gamma(\mathbf{u}) = \mathsf{A}_\Gamma \mathbf{u} - \mathbf{f}_\Gamma = \mathbf{0} \quad \text{on } \Gamma \tag{16}$$

where $\mathbf{r}_\Omega(\mathbf{u})$ and $\mathbf{r}_\Gamma(\mathbf{u})$ are the residual functions in the domain and on the boundary, respectively. To solve the nonlinear problems, Newton's method is employed. Then, the residuals are linearized as follows:

$$\mathrm{D}\mathbf{r}_\Omega(\mathbf{u})[\delta\mathbf{u}] = \mathsf{K}_\Omega \delta\mathbf{u} \quad \text{in } \Omega \tag{17}$$

$$\mathrm{D}\mathbf{r}_\Gamma(\mathbf{u})[\delta\mathbf{u}] = \mathsf{K}_\Gamma \delta\mathbf{u} \quad \text{on } \Gamma \tag{18}$$

where K_Ω and K_Γ represent the directional derivative operators in the domain and on the boundary, respectively. The residuals and unknown function $\mathbf{u}$ can be computed by iterating the following scheme when updating the (k)th iteration step to the $(k+1)$th iteration step:

$$\mathbf{r}_\Omega^{(k)} = \mathsf{A}_\Omega \mathbf{u}^{(k)} - \mathbf{f}_\Omega \tag{19}$$

$$\mathbf{r}_\Gamma^{(k)} = \mathsf{A}_\Gamma \mathbf{u}^{(k)} - \mathbf{f}_\Gamma \tag{20}$$

$$\mathsf{K}_\Omega \delta\mathbf{u} = -\mathbf{r}_\Omega^{(k)} \tag{21}$$

$$\mathsf{K}_\Gamma \delta\mathbf{u} = -\mathbf{r}_\Gamma^{(k)} \tag{22}$$

$$\mathbf{u}^{(k+1)} = \mathbf{u}^{(k)} + \delta\mathbf{u} \tag{23}$$

Both Eqs. (21) and (22) are linear, so $\delta\mathbf{u}$ can be obtained by using a numerical solution of algebraic equations. The operators $\mathbf{r}_\Omega(\mathbf{u})$ and $\mathbf{r}_\Gamma(\mathbf{u})$ are also constructed in each step up to the unknown function $\mathbf{u}^{(k)}$. Most meshless methods based on the particle collocation approach discretize Eqs. (13) and (14) directly for the numerical solution. In contrast, the presented method introduces Eqs. (21) and (22) to extend the point collocation approach so that nonlinear problems can be solved by using the linearization and the iteration scheme.

2.3 Governing equations

In the classical theory of elasticity, the analytical solution for crack problems is obtained to solve the equilibrium equation by imposing boundary conditions on the crack faces. Similarly, the point collocation method can express cracks by imposing the traction boundary condition on the crack faces. Consider a solid mechanics problem with a small deformation in the domain Ω with the crack Γ_c $(\Gamma_{c+}+\Gamma_{c-})$, i.e., bounded by Γ $(\Gamma_t \cup \Gamma_u \cup \Gamma_c)$ as shown in Fig. 2. At each point $\mathbf{x} \in \Omega$, the problem is governed by the following set of differential equations:

$$\mathrm{div}\boldsymbol{\sigma} + \mathbf{b} = \mathbf{0} \quad \text{in } \Omega \tag{24}$$
$$\boldsymbol{\sigma}\mathbf{n} = \mathbf{t} \quad \text{on } \Gamma_t \tag{25}$$
$$\mathbf{u} = \bar{\mathbf{u}} \quad \text{on } \Gamma_u \tag{26}$$
$$\boldsymbol{\sigma}\mathbf{n}_{c+} = \mathbf{t}_{c+} \quad \text{on } \Gamma_{c+} \tag{27}$$
$$\boldsymbol{\sigma}\mathbf{n}_{c-} = \mathbf{t}_{c-} \quad \text{on } \Gamma_{c-} \tag{28}$$

where $\boldsymbol{\sigma}$ is the Cauchy stress tensor; $\mathbf{b}$ is the body force; $\mathbf{n}$, $\mathbf{n}_{c+}$, and $\mathbf{n}_{c-}$ are the outward surface normal vectors; $\mathbf{t}$ and $\mathbf{t}_{c+} = -\mathbf{t}_{c-}$ are the tractions; and $\bar{\mathbf{u}}$ is the prescribed displacement. This means that Eq. (14) directly applies to not only Γ_t but also Γ_c. In other words, the boundary condition of cracks is simply embodied by the addition of nodes on crack faces and by imposing a node-wise strong formulation. Then, the residual functions are given as

$$\mathbf{r}_\Omega = \mathrm{div}\boldsymbol{\sigma} + \mathbf{b} \quad \text{in } \Omega \tag{29}$$
$$\mathbf{r}_{\Gamma_t} = \boldsymbol{\sigma}\mathbf{n} - \mathbf{t} \quad \text{on } \Gamma_t \tag{30}$$
$$\mathbf{r}_{\Gamma_u} = \mathbf{u} - \bar{\mathbf{u}} \quad \text{on } \Gamma_u \tag{31}$$
$$\mathbf{r}_{\Gamma_{c+}} = \boldsymbol{\sigma}\mathbf{n}_{c+} - \mathbf{t}_{c+} \quad \text{on } \Gamma_{c+} \tag{32}$$
$$\mathbf{r}_{\Gamma_{c-}} = \boldsymbol{\sigma}\mathbf{n}_{c-} - \mathbf{t}_{c-} \quad \text{on } \Gamma_{c-} \tag{33}$$

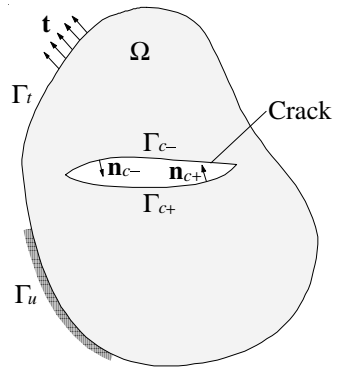

Figure 2: Schematic drawing of a cracked body

and the linearization is derived as

$$\left[\mathrm{D}\mathbf{r}_{\Omega}[\delta\mathbf{u}]\right]_i = \frac{\partial \mathsf{D}_{ijkl}}{\partial x_j}\frac{\partial^s \delta u_k}{\partial^s x_l} + \mathsf{D}_{ijkl}\frac{\partial}{\partial x_j}\frac{\partial^s \delta u_k}{\partial^s x_l} \quad \text{in } \Omega \tag{34}$$

$$\mathrm{D}\mathbf{r}_{\Gamma_t}[\delta\mathbf{u}] = (\mathsf{D} : \nabla^s \delta\mathbf{u})\mathbf{n} \quad \text{on } \Gamma_t \tag{35}$$

$$\mathrm{D}\mathbf{r}_{\Gamma_u}[\delta\mathbf{u}] = \delta\mathbf{u} \quad \text{on } \Gamma_u \tag{36}$$

$$\mathrm{D}\mathbf{r}_{\Gamma_{c+}}[\delta\mathbf{u}] = (\mathsf{D} : \nabla^s \delta\mathbf{u})\mathbf{n}_{\mathbf{c}+} - \mathrm{D}\mathbf{t}_{c+}[\delta\mathbf{u}] \quad \text{on } \Gamma_{c+} \tag{37}$$

$$\mathrm{D}\mathbf{r}_{\Gamma_{c-}}[\delta\mathbf{u}] = (\mathsf{D} : \nabla^s \delta\mathbf{u})\mathbf{n}_{\mathbf{c}-} - \mathrm{D}\mathbf{t}_{c-}[\delta\mathbf{u}] \quad \text{on } \Gamma_{c-} \tag{38}$$

where the summation convention is applied in Eq. (34) and D is called a tangent modulus tensor. The operator ∇^s is defined as

$$\nabla^s \delta\mathbf{u} = \frac{\partial^s \delta u_i}{\partial^s x_j} = \frac{1}{2}\left(\frac{\partial \delta u_i}{\partial x_j} + \frac{\partial \delta u_j}{\partial x_i}\right) \tag{39}$$

with the summation convention. The tangent modulus for the isotropic elastic material is written by

$$\mathsf{D} = 2G\mathsf{I}_d + K\mathbf{I}\otimes\mathbf{I} \tag{40}$$

where K is the bulk modulus, G is the transverse elasticity modulus, I_d is the deviatoric projection tensor, and $\mathbf{I}$ is the identity tensor. By discretizing Eqs. (29)–(38) through the C-MLS approximation, linear algebraic equations related to Eqs. (21) and (22) for the iteration procedure are obtained from

$$\mathbf{K}\delta\mathbf{u} = -\mathbf{r} \tag{41}$$

where $\mathbf{K}$ is a coefficient matrix (i.e., Jacobian matrix) and $\mathbf{r}$ is the residual vector. When the (k)th step is updated to the $(k+1)$th step in the iteration for Newton's method, the above formulation is decomposed as

$$\begin{bmatrix} \mathbf{K}_{\Omega} \\ \mathbf{K}_{\Gamma_t} \\ \mathbf{K}_{\Gamma_u} \\ \mathbf{K}_{\Gamma_{c+}} \\ \mathbf{K}_{\Gamma_{c-}} \end{bmatrix} \begin{pmatrix} \delta\mathbf{u}_{\Omega} \\ \delta\mathbf{u}_{\Gamma_t} \\ \delta\mathbf{u}_{\Gamma_u} \\ \delta\mathbf{u}_{\Gamma_{c+}} \\ \delta\mathbf{u}_{\Gamma_{c-}} \end{pmatrix} = - \begin{pmatrix} \mathbf{r}_{\Omega}^{(k)} \\ \mathbf{r}_{\Gamma_t}^{(k)} \\ \mathbf{r}_{\Gamma_u}^{(k)} \\ \mathbf{r}_{\Gamma_{c+}}^{(k)} \\ \mathbf{r}_{\Gamma_{c-}}^{(k)} \end{pmatrix} \tag{42}$$

where $\mathbf{r}_{\Omega}^{(k)}$, $\mathbf{r}_{\Gamma_t}^{(k)}$, $\mathbf{r}_{\Gamma_u}^{(k)}$, $\mathbf{r}_{\Gamma_{c+}}^{(k)}$, $\mathbf{r}_{\Gamma_{c-}}^{(k)}$, $\mathbf{K}_{\Omega}$, $\mathbf{K}_{\Gamma_t}$, $\mathbf{K}_{\Gamma_u}$, $\mathbf{K}_{\Gamma_{c+}}$, and $\mathbf{K}_{\Gamma_{c-}}$ are sub-matrices obtained by the discretization of Eqs. (29)–(38), respectively. In particular, $\mathbf{K}_{\Gamma_u}$ is simply expressed as follows owing to the C-MLS approximation:

$$\mathbf{K}_{\Gamma_u} = \begin{bmatrix} \mathbf{0} & \mathbf{I} & \mathbf{0} \end{bmatrix} \tag{43}$$

where the elements of $\mathbf{I}$ are located corresponding to $\delta\mathbf{u}_{\Gamma_u}$. The coefficient matrix is sparse and banded but is generally non-symmetric because it is based on the strong formulation. Equation (41) should be linearly independent so as not to cause singularity of the coefficient matrix.

The steps of the method for updating the time step t_n to t_{n+1} are written below:

Phase 1. Construct the coefficient matrix $\mathbf{K}$ of discretized Eqs. (34)–(38).

Phase 2. Obtain $\delta\mathbf{u}$ by using the numerical solution for Eq. (41) and update the displacement $\mathbf{u}_{n+1}^{(k)}$ to $\mathbf{u}_{n+1}^{(k+1)}$ for the $(k+1)$th iteration step given by Eq. (23).

Phase 3. Update the stress $\boldsymbol{\sigma}_{n+1}^{(k+1)}$ and traction on the crack faces $\mathbf{t}_{c+} = -\mathbf{t}_{c-}$.

Phase 4. Compute the residual vector $\mathbf{r}_{n+1}^{(k+1)}$ by using discretized Eqs. (29)–(33).

Phase 5. If the convergence criteria are satisfied, end the iteration and take the next time step; otherwise, continue the iteration by returning to Phase 1.

The shape function approximated by C-MLS is constructed only once before the above procedure because of the hypothesis of a small deformation. Newton's method is widely used to solve nonlinear problems, so this procedure has a framework based on Newton's method that is basically common to conventional numerical methods such as the finite element method (FEM). However, the coefficient matrix and linear algebraic equations derived from the strong-form governing equations distinctly differ from those employed in FEM when the weak form is assumed. Hence, the presented method, which needs no meshes or numerical integration, can achieve a simpler scheme and reduce the computational costs for iterations.

2.4 Crack propagation modeling

In order to deal with the displacement discontinuity due to cracks, the so-called visibility criterion [19] used in other meshless methods is employed with the C-MLS approximation. In contrast to the conventional FEM, the meshless interpolation procedure used in meshless methods such as MLS can adjust the size and shape of its domain of influence for the crack discontinuity. The visibility criterion simply cuts through the domain of influence and ignores the nodes placed at the opposite side of the crack, as shown in Fig. 3. As a result, the C-MLS approximation modified by the visibility criterion allows the displacement field to contain jump discontinuities across the crack face.

Most other meshless methods employ a special function in the approximation to deal with the singularity of the stress field near the crack tip [19], but there have been few reports suggesting a special function that can be applied to complex three-dimensional singularity. In this work, the solution at the concave corner including the crack tip is defined by superposition of multiple nodal solutions. As an example, the methodology for the two-dimensional case is depicted in Fig. 4 (a). Consider the concave corner node and two lines modeling surfaces Γ_1 and Γ_2 with outward normal vectors $\mathbf{n}_1$ and $\mathbf{n}_2$, respectively. Assume that the natural boundary condition of the concave corner node is approximated by the following average:

$$\boldsymbol{\sigma}_1\mathbf{n}_1 + \boldsymbol{\sigma}_2\mathbf{n}_2 = \mathbf{t}_1 + \mathbf{t}_2 \tag{44}$$

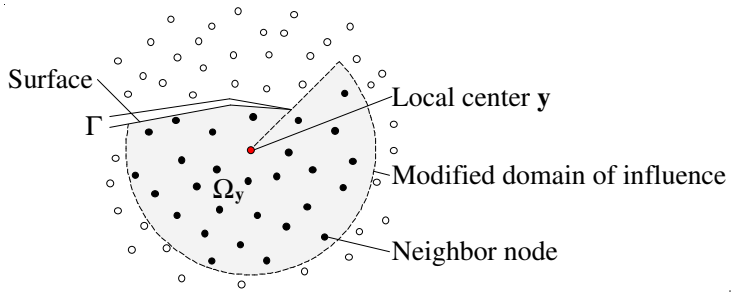

Figure 3: Modification of the domain of influence by the visibility criterion

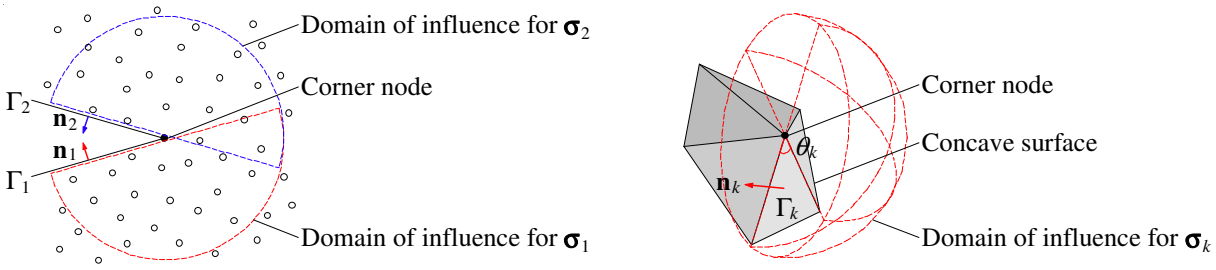

(a) two dimensions (b) three dimensions

Figure 4: Corner node located at concave boundary surfaces

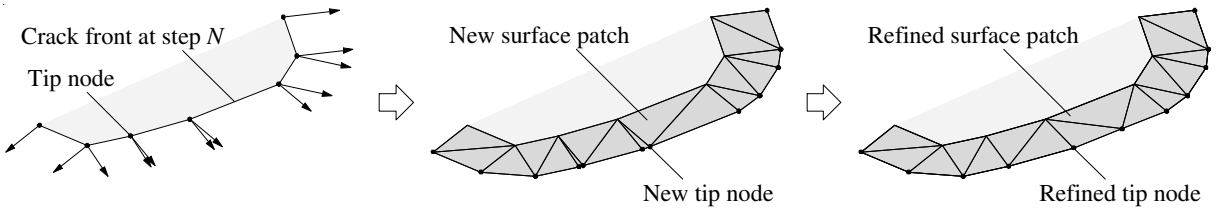

(a) Locate new tip nodes (b) Extend crack front at step N+1 (c) Refine crack front at step N+1

Figure 5: Crack propagation modeled in surface patches and tip nodes

where $\mathbf{n}_1$ and $\mathbf{n}_2$ are the surface tractions. The stress $\boldsymbol{\sigma}_1$ and $\boldsymbol{\sigma}_2$ are computed by using shape functions approximated by C-MLS with the visibility criterion corresponding to each surface. These are derived for each domain of influence, as shown in Fig. 4 (a). In three dimensions, the crack faces is represented by a polyhedron with triangle patches, as illustrated in Fig. 4 (b), and approximate the natural boundary condition of the concave corner node as the following extension of the two-dimensional case:

$$\sum_{k=1}^{n} \theta_k \boldsymbol{\sigma}_k \mathbf{n}_k = \sum_{k=1}^{n} \theta_k \mathbf{t}_k \tag{45}$$

where n is the number of surface patches around the corner node and θ_k, $\boldsymbol{\sigma}_k$, $\mathbf{n}_k$, and $\mathbf{t}_k$ are the angle between two sides, the stress, and the traction corresponding to each surface patch. When using individual nodal values, the stress at the corner node is represented by $\boldsymbol{\sigma} = (\sum_{k=1}^{n} \theta_k \boldsymbol{\sigma}_k \mathbf{n}_k)/(\sum_{k=1}^{n} \theta_k)$. The above procedure is similar to the treatment for the natural boundary condition at the corner in the finite difference method (FDM) in terms of averaging the directional derivatives for the surface patches to obtain the approximation. The accuracy of this procedure for the singularity of a crack tip was tested in an example described below.

Next, the procedure of crack propagation is explained. The point collocation method is a truly meshless method based on a strong formulation. Thus, geometric changes to the analysis model, such as the addition and subtraction of nodes and surfaces, are applied more easily than in conventional mesh methods. As shown in Fig. 5, the crack front is composed of tip lines and tip nodes on a collection of surface patches representing crack faces. Crack propagation is defined as the motion of the crack front. The advance of the crack front is expressed by the locations of the newly added tip nodes, and the direction of the crack propagation is assumed according to the maximum principal stress. For each tip node, the direction of crack propagation is defined as perpendicular to the direction of the maximum principal stress and the direction along the tip line. In other words, two direction corresponding to the tip lines

are defined, and two new tip nodes are generated for each tip node. The length of the crack growth d_c for each increment is predefined as a sufficiently small value to simulate the actual crack shape. Once the positions of the new tip nodes are determined, the crack faces need to be updated. This is easily done in two dimensions by the addition of tip lines. In three dimensions, a series of surface patches is constructed. In addition, the surface patches are refined if the crack front edge is too long or too short. Specifically, a crack edge that is longer or shorter than the user-specified threshold is subdivided or deleted, as shown in Fig. 5. Most conventional mesh methods have difficulty with applying the above geometric changes due to crack propagation because the change in a system based on the weak formulation causes additional features to be implemented. For instance, the change in element formulation due to the addition and subtraction of nodes, consistency between the mesh connectivity and continuity of the fracture zone location, and others need to be considered. In contrast, the presented method maintains simplicity and effectiveness due to the strong formulation. Therefore, this is a significant advantage of the presented method for dealing with crack propagation.

2.5 Fracture criterion and cohesive crack model

This section describes the physical model of the crack propagation. The presented method employs a Rankine-type fracture criterion where the crack is assumed to be initiated when the maximum principal stress exceeds the uniaxial tensile strength. The crack face is introduced perpendicular to the direction of the maximum principal stress, as noted previously. For some geomaterials such as concrete, this provides sufficiently accurate results if no significant lateral compression is present [20].

When the fracture criterion is met, discrete crack faces are introduced by adding the surface patches and nodes. Then, a cohesive crack model is assumed, i.e., cohesive traction is applied along newly generated crack faces. In other words, the crack faces of the model represent the interface between the cohesive zone and the surrounding material. The cohesive traction depends on a cohesive law that relates the traction to the jump in displacement across the discontinuity of the crack faces. The relative displacement across the crack faces is represented by

$$\boldsymbol{w}_c = \mathbf{x}_{c-} - \mathbf{x}_{c+} \tag{46}$$

where $\mathbf{x}_{c+}$ and $\mathbf{x}_{c-}$ are the positions of the nodes on the pair of surface patches. In this work, only the normal component of the cohesive traction was considered. The cohesive traction prescribed on the surface patch Γ_{c+} is written as follows:

$$\mathbf{t}_{c+} = t_c(w_c)\mathbf{n}_{c+} \tag{47}$$

where $\mathbf{t}_{c+} = -\mathbf{t}_{c-}$ is the cohesive traction on Γ_{c+}, $t_c(w_c)$ is the cohesive traction force determined by the cohesive law, w_c is the normal component of $\boldsymbol{w}_c$, and $\mathbf{n}_{c+}$ is the surface normal. The cohesive traction is linearized as follows:

$$\mathrm{D}\mathbf{t}_{c+}[\delta\mathbf{u}] = \frac{\partial t_c}{\partial w_c}\left(\mathbf{n}_{c+} \otimes \mathbf{n}_{c+}\right)\delta\boldsymbol{w}_c \tag{48}$$

where $\partial t_c/\partial w_c$ is the modulus computed by the cohesive law. In this study, an exponential cohesive law was employed. As shown in Fig. 6, the energy dissipated by the development of the crack opening matches the fracture energy. Thus, t_c is related to w_c by the following softening relationship:

$$t_c(w_c) = f_t \exp\left(-\frac{f_t}{G_f} w_c\right) \tag{49}$$

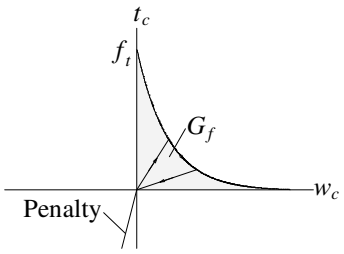

Figure 6: Schematic drawing of the exponential cohesive law

where G_f is the specific fracture energy of the material and f_t indicates the traction force at failure. In addition, note that a penalty force is introduced to consider the crack surface overlap. Most conventional methods apply the cohesive crack model to the material constitutive law to easily treat the discontinuity. In contrast, the presented method directly expresses the framework of the cohesive crack model because the crack surfaces and cohesive traction are simply introduced in combination with the crack growth procedure. Particularly in this regard, the presented method is attractive for the analysis of brittle and quasi-brittle fracture.

3 NUMERICAL EXAMPLES

3.1 Near-tip crack field problem

A patch test for a singular field was performed. A closed-form solution for a crack can be derived by using the known near-tip field in a domain about the crack tip. A cuboid region was considered as shown in Fig. 7, and the known near-tip displacement fields from the solution for a mode I crack were prescribed along the boundaries parallel to the tip line. Symmetric boundary conditions were imposed on the surfaces perpendicular to the tip line to assume the plane strain condition, and traction-free boundary conditions were applied to the crack faces. This example is an intrinsically two-dimensional problem, and the displacement for the near-tip field is given by

$$u_x = \frac{K_I}{2G}\sqrt{\frac{r}{2\pi}}\cos\left(\frac{\theta}{2}\right)\left[\kappa - 1 + 2\sin^2\left(\frac{\theta}{2}\right)\right] \tag{50}$$

$$u_z = \frac{K_I}{2G}\sqrt{\frac{r}{2\pi}}\sin\left(\frac{\theta}{2}\right)\left[\kappa + 1 - 2\cos^2\left(\frac{\theta}{2}\right)\right] \tag{51}$$

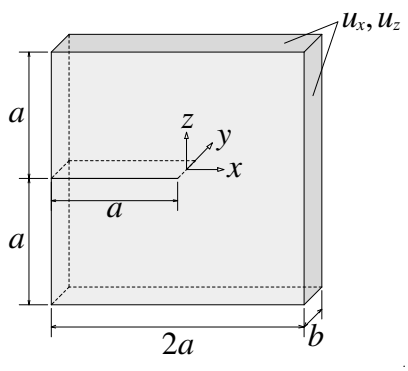

Figure 7: Cuboid region for a near-tip crack problem

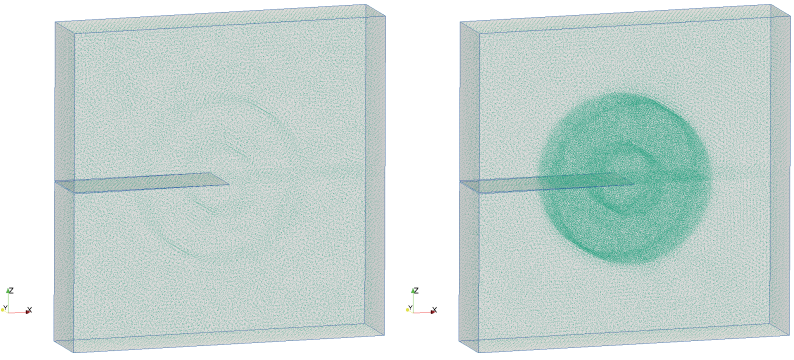

(a) 95,335 nodes (b) 206,195 nodes

Figure 8: Node distribution for a near-tip crack problem

Table 1: Recalculated stress intensity factors for a near-tip crack problem

Case	Number of nodes	Node density	Recalculated SIFs	Relative error (%)
1	15,160	Homogeneous	0.99059	0.94
2	95,335	Homogeneous	0.99789	0.21
3	300,514	Homogeneous	1.00256	0.26
4	206,195	Heterogeneous	1.00005	0.01

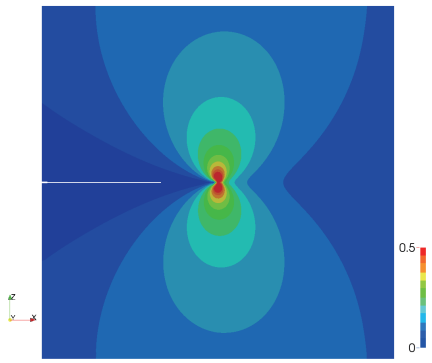

Figure 9: Von Mises stress in the section at $y = 0$ for a near-tip crack problem

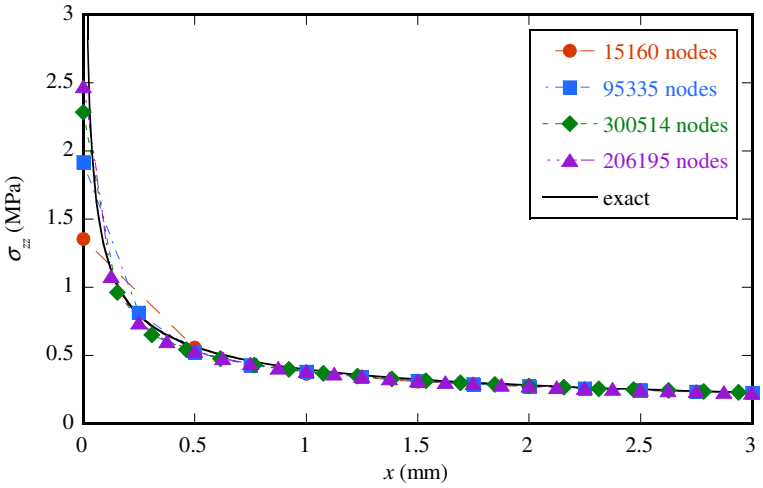

Figure 10: Distribution of the normal stress σ_{zz} for the near-tip field along the line $y = z = 0$ for a near-tip crack problem

where r is the distance from the crack tip line in the cylindrical coordinate system, θ is the angle measured from the line ahead of the crack, K_I is the stress intensity factor, and κ is the Kolosov constant defined as $\kappa = 3 - 4\nu$ for the plane strain [21]. The parameters of $a = 10$ mm, $b = 4$ mm, $K_I = 1$ MPa $\cdot$ mm$^{1/2}$, Young's modulus $E = 200$ GPa, and Poisson's ratio $\nu = 0.3$ were used. For the convergence test, four cases for the number of nodes given in Table 1 were used. As shown in Fig. 8, irregular patterns of the node distribution were adopted for each case. The node density of the case with 206,195 nodes was locally refined near the crack tip, and the others were nearly homogeneous.

Table 1 provides the stress intensity factors (SIFs) for the numerical results recalculated by the M-integral method [22], and Fig. 9 illustrates the von Mises stress distribution in a section of $y = 0$ for the case with 206,195 nodes. The recalculated SIFs showed good agreement with the prescribed value in every case. In addition, Fig. 10 plots the numerical results for the distribution of normal stress σ_{zz} ahead of the crack tip along the line of $y = x = 0$ with the exact solution. The results indicated that the modeling approach described above worked successfully, even though the near-tip field was not enriched to capture the stress singularity at the crack tip strictly. Furthermore, it is confirmed that the C-MLS approximation provides the accurate numerical results as well as other meshless approximations.

3.2 Double-edge notched specimen under tension

The second example was the simple fracture analysis of a uniaxial tension test on a double-edge notched (DEN) specimen. The geometry and prescribed boundary conditions are illustrated in Fig. 11. The specimen was weakened by two notches to initialize fracture. Because

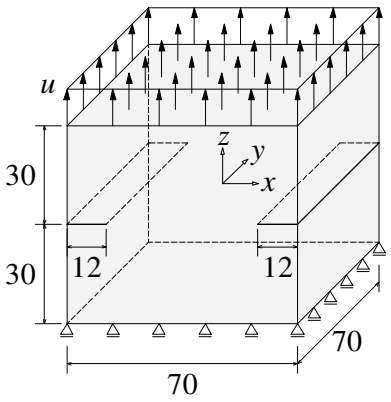

Figure 11: Geometry and applied boundary conditions for a DEN test

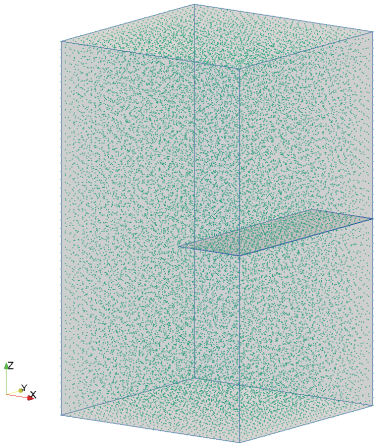

Figure 12: Node distribution for a DEN test

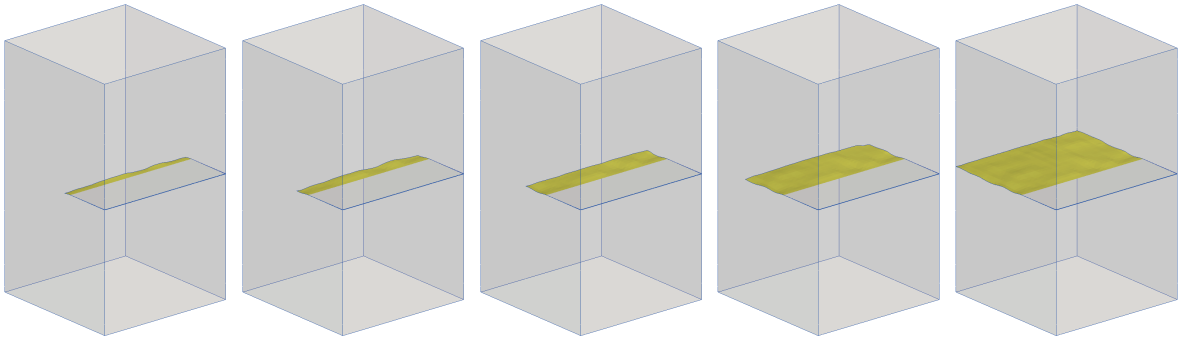

(a) $u = 1.6$ µm (b) $u = 2.4$ µm (c) $u = 3.2$ µm (d) $u = 4.0$ µm (e) $u = 4.8$ µm

Figure 13: Crack propagation for a DEN test

of the symmetry, one quarter of the specimen was discretized with proper symmetric boundary conditions, as displayed in Fig. 12. This also implies that the symmetry of the crack propagation was enforced. The numerical simulation was carried out for the irregular node distribution of 23,988 nodes and the crack increment length of $d_c = 1.04$ mm. The material parameters were taken to be equivalent to those of Comi et al. [23] as follows: $E = 36$ GPa, $\nu = 0.1$, $f_t = 3.0$ MPa and $G_f = 0.011$ N/mm. A displacement control procedure was employed based on the uniform displacement in the z-direction u prescribed on the top of the specimen.

Fig. 13 depicts the resulting crack evolution and Fig. 14 provides the maximum principal stress distribution where the displacements are scaled by a factor of 100. Two planar cracks extended from each notch until they joined within the specimen, and the specimen was completely cut by the crack at the end. Note that the fracture process can be nonsymmetric if the symmetric property is not considered because a possible scenario is that only one of the two cracks extends while the other crack unloads owing to the material imperfection. Fig. 15 compares the load–displacement response with the numerical results obtained by using the extended finite element method (XFEM) with a continuum damage model [23]. Both response curves had a rapid drop after the peak load, although the falls in the load after the rapid drop were different. The numerical results of the presented method seem to qualitatively agree with the experimental results [24].

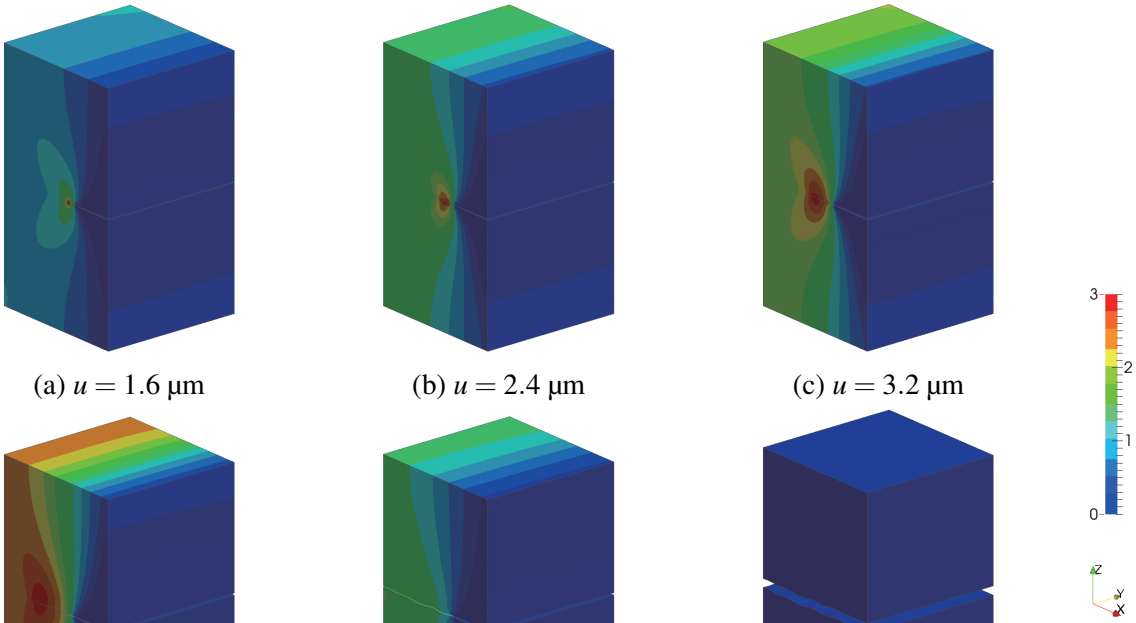

(a) $u = 1.6$ µm (b) $u = 2.4$ µm (c) $u = 3.2$ µm

(d) $u = 4.0$ µm (e) $u = 4.8$ µm (f) $u = 20.0$ µm

Figure 14: Maximum principal stress for a DEN test

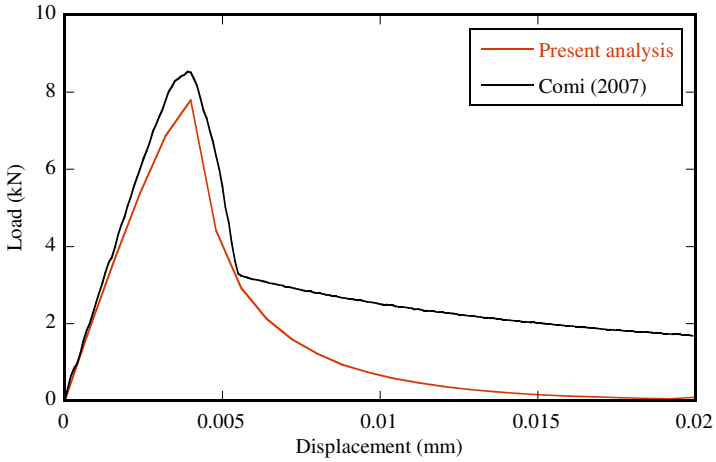

Figure 15: Reaction load versus prescribed displacement for a DEN test

3.3 Anchor pull-out test

The next example was the pull-out test of a steel anchor embedded in a cylindrical concrete block. The dimensions and material parameters were set to $E = 30$ GPa, $\nu = 0.2$, $f_t = 3.0$ MPa, and $G_f = 0.106$ N/mm, which are similar to those used by Rots [20] and Gasser and Holzapfel [25]. Fig. 16 displays a quarter of the geometric data and applied boundary conditions. A vertical load F was imposed on the center of the steel disk, and the embedded disc was pulled against a counter pressure placed concentric with the disc on the surface until the

surrounding concrete fractured. As shown in Fig. 17, a quarter of the whole structure was modeled, and symmetric boundary conditions were applied. Note that the three-dimensional model was used in this work to investigate the presented method in three dimensions, although this problem is intrinsically axisymmetric and can be modeled more simply. The irregular node distribution of 23,232 nodes and crack increment length of $d_c = 18$ mm were used. The steel anchor was not explicitly modeled; instead, an incremental displacement u in the z-direction was prescribed at the nodes of the upper contact surface between the steel disc and concrete by assuming that the steel disc was rigid. The numerical analysis is conducted under displacement control; a constant incremental displacement of 0.025 mm was imposed in each load step until

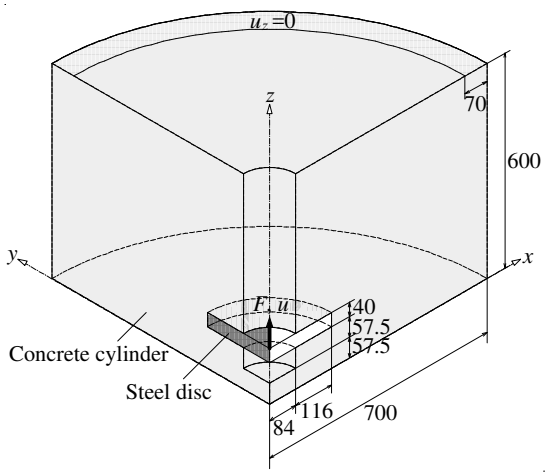

Figure 16: Geometry and applied boundary conditions for an anchor pull-out test

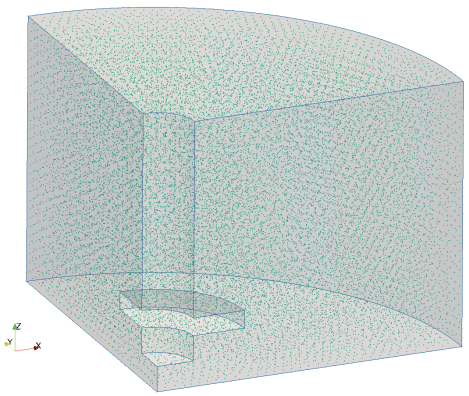

Figure 17: Node distribution for an anchor pull-out test

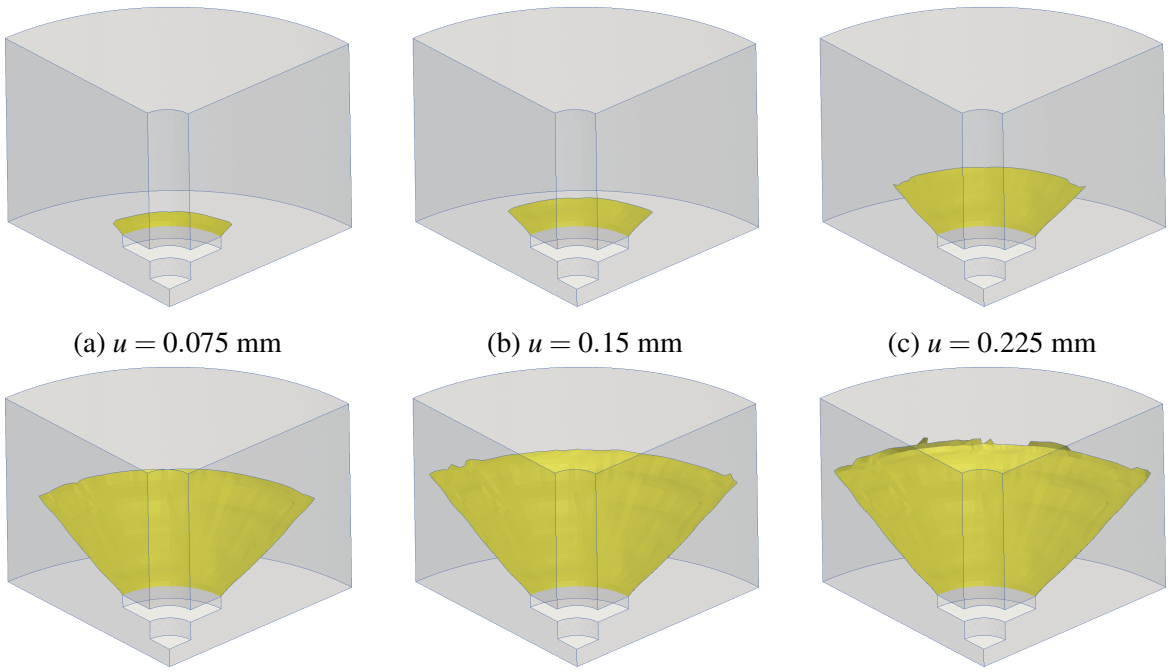

(a) $u = 0.075$ mm (b) $u = 0.15$ mm (c) $u = 0.225$ mm

(d) $u = 0.275$ mm (e) $u = 0.35$ mm (f) $u = 0.4$ mm

Figure 18: Crack propagation for an anchor pull-out test

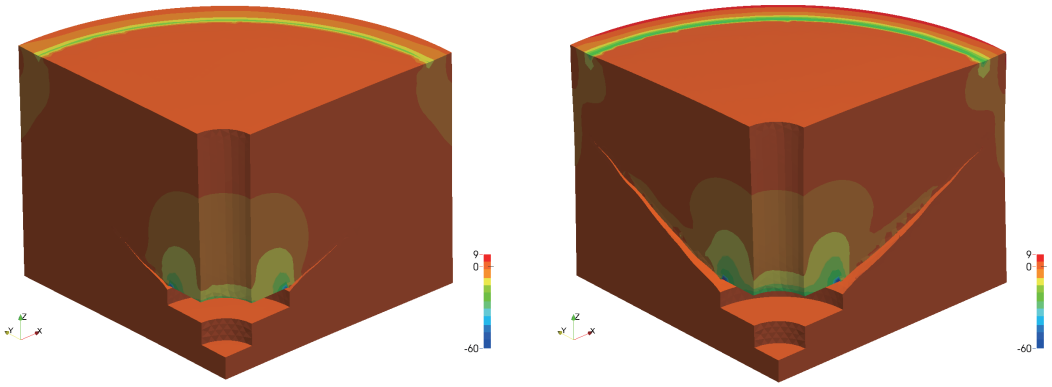

(a) $u = 0.225$ mm (b) $u = 0.4$ mm

Figure 19: Normal stress in the loading direction σ_{zz} for an anchor pull-out test

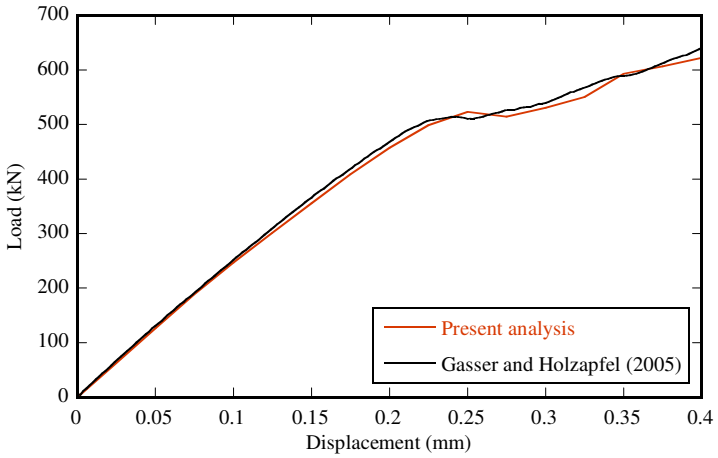

Figure 20: Reaction load versus prescribed displacement for an anchor pull-out test

the displacement reached the final value of 0.4 mm.

Fig. 18 depicts the propagating crack surface of the concrete cylinder, where the different stages are associated with different levels of prescribed displacements. The crack initiated from the outer edge of the upper contact surface of the steel disc into the concrete, and the final crack surface exhibited a conical shape similar to those observed in the experimental results [20] and numerical results of the literature [25]. Fig. 19 shows the normal stress distribution plotted on the deformed representation corresponding to the results of the load steps at the applied displacements $u = 0.225$ mm and $u = 0.4$ mm, respectively. Finally, Fig. 20 shows the evolution of the corresponding load versus the prescribed displacement, where the resulting curve is compared with the numerical result from Gasser and Holzapfel [25] using PUFEM. The load–displacement curve was almost linear until a load of about 500 kN was reached. Afterwards, there was a short drop in the reaction load with an acceleration of the succeeding crack propagation. The accelerated crack growth ended when the crack front reached below the ring zone to which the displacement boundary condition $u_z = 0$ was applied. Finally, the load increased again when the displacement went beyond about 0.28 mm. Both the aforementioned phenomena and load–displacement response showed good agreement with the numerical results in the literature [25].

4 CONCLUSIONS

This paper presents a meshless point collocation method for three-dimensional crack propagation. The presented method yields a truly meshless fracture analysis by using C-MLS approximation, node-wise discretization based on the strong formulation, and crack propagation represented by the addition of nodes and surfaces. The C-MLS approximation provides derivative approximations without direct differentiation and does not require any special implementation to treat essential boundary conditions. The geometric change due to crack growth is simply represented by the addition and subtraction of nodes and surfaces, and the cohesive crack model is employed in association with the crack propagation procedure to directly embody the fracture of quasi-brittle materials in a sufficient manner. Numerical examples were performed to demonstrate the accuracy and effectiveness of the presented method. This method has the potential to solve other problems involving geometric and boundary nonlinearity, such as large deformations.

REFERENCES

[1] L. B. Lucy, A numerical approach to the testing of the fission hypothesis, Astronom. J. 82 (1977) 1013–1024.

[2] R. A. Gingold, J. J. Monaghan, Smoothed particle hydrodynamics: theory and application to non-spherical stars, Mon. Not. R. Astron. Soc. 181 (3) (1977) 375–389.

[3] B. Nayroles, G. Touzot, P. Villon, Generalizing the finite element method: diffuse approximation and diffuse elements, Comput. Mech. 10 (5) (1992) 307–318.

[4] T. Belytschko, Y. Y. Lu, L. Gu, Element-free Galerkin methods, Int. J. Numer. Meth. Eng. 37 (2) (1994) 229–256.

[5] W. K. Liu, S. Jun, S. Li, J. Adee, T. Belytschko, Reproducing kernel particle methods for structural dynamics, Int. J. Numer. Meth. Eng. 38 (10) (1995) 1655–1679.

[6] J. M. Melenk, I. Babuška, The partition of unity finite element method: basic theory and applications, Comput. Meth. Appl. Mech. Eng. 139 (1) (1996) 289–314.

[7] P. Lancaster, K. Salkauskas, Surfaces generated by moving least squares methods, Math. Comp. 37 (155) (1981) 141–158.

[8] E. Onate, S. Idelsohn, O. Zienkiewicz, R. Taylor, A finite point method in computational mechanics. Applications to convective transport and fluid flow, Int. J. Numer. Meth. Eng. 39 (22) (1996) 3839–3866.

[9] N. Aluru, A point collocation method based on reproducing kernel approximations, Int. J. Numer. Meth. Eng. 47 (6) (2000) 1083–1121.

[10] Y.-C. Yoon, J.-H. Song, Extended particle difference method for weak and strong discontinuity problems: part I. Derivation of the extended particle derivative approximation for the representation of weak and strong discontinuities, Comput. Mech. 53 (6) (2014) 1087–1103.

[11] E. Oñate, F. Perazzo, J. Miquel, A finite point method for elasticity problems, Comput. Struct. 79 (22) (2001) 2151–2163.

[12] L. P. Pozo, F. Perazzo, A. Angulo, A meshless FPM model for solving nonlinear material problems with proportional loading based on deformation theory, Adv. Eng. Softw. 40 (11) (2009) 1148–1154.

[13] W. Tu, Y. Gu, P. Wen, Effective shear modulus approach for two dimensional solids and plate bending problems by meshless point collocation method, Eng. Anal. Boundary Elem. 36 (5) (2012) 675–684.

[14] S.-H. Lee, Y.-C. Yoon, Meshfree point collocation method for elasticity and crack problems, Int. J. Numer. Meth. Eng. 61 (1) (2004) 22–48.

[15] H. Noguchi, T. Noguchi, Application of new gridless method using least square method with constraint condition to structural problems, in: Proceedings of the Conference on Computational Engineering and Science, Vol. 2, 1997, pp. 391–394.

[16] H. Minaki, H. Noguchi, Large deformation elastic-plastic analysis by SMAC-SPH using constrained moving least squares method, in: The Computational Mechanics Conference, Vol. 2005, 2005, pp. 763–764.

[17] G. Barenblatt, The formation of equilibrium cracks during brittle fracture. General ideas and hypotheses. Axially-symmetric cracks, J. Appl. Math. Mech. 23 (3) (1959) 622–636.

[18] D. W. Kim, H.-K. Kim, Point collocation method based on the FMLSRK approximation for electromagnetic field analysis, IEEE Trans. Magn. 40 (2) (2004) 1029–1032.

[19] M. Fleming, Y. Chu, B. Moran, T. Belytschko, Y. Lu, L. Gu, Enriched element-free Galerkin methods for crack tip fields, Int. J. Numer. Meth. Eng. 40 (8) (1997) 1483–1504.

[20] J. G. Rots, Computational modeling of concrete fracture, Ph.D. thesis, Delft University of Technology (1988).

[21] M. Williams, On the stress distribution at the base of a stationary crack, J. Appl. Mech. 24 (1957) 109–114.

[22] J. Yau, S. Wang, An analysis of interface cracks between dissimilar isotropic materials using conservation integrals in elasticity, Eng. Fract. Mech. 20 (3) (1984) 423–432.

[23] C. Comi, S. Mariani, U. Perego, An extended fe strategy for transition from continuum damage to mode I cohesive crack propagation, Int. J. Numer. Anal. Methods Geomech. 31 (2) (2007) 213–238.

[24] D. A. Hordijk, Local approach to fatigue of concrete, Ph.D. thesis, TU Delft, Delft University of Technology (1991).

[25] T. C. Gasser, G. A. Holzapfel, Modeling 3D crack propagation in unreinforced concrete using PUFEM, Comput. Meth. Appl. Mech. Eng. 194 (25) (2005) 2859–2896.